CONTRAST MEDIA & MOLECULAR IMAGING

Received: 13 August 2015, Revised: 6 October 2015, Accepted: 27 November 2015, Published online in Wiley Online Library: 8 January 2016

(wileyonlinelibrary.com) DOI: 10.1002/cmmi.1681

Fast synthesis and bioconjugation of ^{68}Ga core-doped extremely small iron oxide nanoparticles for PET/MR imaging

Juan Pellico[a,b], Jesús Ruiz-Cabello[a,b], Marina Saiz-Alía[a], Gilberto del Rosario[c], Sergio Caja[a], María Montoya[a], Laura Fernández de Manuel[a], M. Puerto Morales[d], Lucia Gutiérrez[d], Beatriz Galiana[e], Jose A. Enríquez[a] and Fernando Herranz[a]*

Combination of complementary imaging techniques, like hybrid PET/MRI, allows protocols to be developed that exploit the best features of both. In order to get the best of these combinations the use of dual probes is highly desirable. On this sense the combination of biocompatible iron oxide nanoparticles and 68Ga isotope is a powerful development for the new generation of hybrid systems and multimodality approaches. Our objective was the synthesis and application of a chelator-free 68Ga-iron oxide nanotracer with improved stability, radiolabeling yield and *in vivo* performance in dual PET/MRI. We carried out the core doping of iron oxide nanoparticles, without the use of any chelator, by a microwave-driven protocol. The synthesis allowed the production of extremely small (2.5 nm) 68Ga core-doped iron oxide nanoparticles. The microwave approach allowed an extremely fast synthesis with a 90% radiolabeling yield and T1 contrast in MRI. With the same microwave approach the nano-radiotracer was functionalized in a fast and efficient way. We finally evaluated these dual targeting nanoparticles in an angiogenesis murine model by PET/MR imaging. Copyright © 2016 John Wiley & Sons, Ltd.

Additional supporting information may be found in the online version of this article at the publisher's web site.

Keywords: chelator-free ^{68}Ga; Iron Oxide; PET/MRI; nano-radiotracer; T_1-MRI

1. INTRODUCTION

Since the advent of medical imaging using nanoparticulate tracers, multimodality has been acclaimed as one of the most advantageous features of these compounds.(1,2). Combination of complementary imaging techniques allows protocols to be developed that exploit the best features of both (e.g., spatial resolution, quantitative and sensitivity), and hybrid positron emission tomography/magnetic resonance imaging scanners (PET/MRI) combining functional and anatomical information are already commercially available (3). However the incorporation of multifunctionality for imaging presents some inherent problems, particularly the multiple synthetic steps needed. These steps increase costs and have many times deleterious effects on the physicochemical properties of the nanoparticles (4). Because of this the design of synthetic schemes minimizing the number of steps to obtain multifunctionality and bioconjugation are necessary. The design of dual-modality PET/MRI nanoscale systems presents at least two key questions: which radioisotope and biocompatible nanocarrier to use, and where the radioisotope will be attached to the engineered agent. In this regard examples have been shown with the use of liposomes and long half-life isotopes (5), quantum dots (6) and gold nanoparticles (7). For multimodal imaging and translationally oriented applications, a particularly attractive radioisotope-nanomaterial combination is Gallium-68 and iron oxide. Gallium-68 is a positron-emitting radionuclide with a relatively short half-life (68 minutes) that makes it ideal for limited dose exposure of patients; another advantage is that ^{68}Ga is produced in a radionuclide generator, allowing synthesis in bench modules and avoiding the need for a cyclotron (8,9). The use of iron oxide nanoparticles for MRI is well-known, particularly as negative contrast in T_2 weighted MRI. However for imaging purposes the use of positive (T_1) contrast enhancement is many times more convenient. This fact has driven the search for magnetic particles or acquisition methods that are able to produce positive, T_1-weighted based contrast (10–16). Reported examples of small iron oxide nanoparticles (IONP) were produced by

* *Correspondence to: F. Herranz, Centro Nacional de Investigaciones Cardiovasculares Carlos III (CNIC). C/ Melchor Fernández-Almagro 3. 28029 Madrid, Spain. E-mail: fherranz@cnic.es*

a *J. Pellico, J. Ruiz-Cabello, M. Saiz-Alía, S. Caja, M. Montoya, L. Fernández de Manuel, J. A. Enríquez, F. Herranz*
Centro Nacional de Investigaciones Cardiovasculares Carlos III (CNIC), C/ Melchor Fernández-Almagro 3. 28029 Madrid Spain

b *J. Pellico, J. Ruiz-Cabello*
Universidad Complutense de Madrid and CIBERES, 28040 Madrid, Spain

c *G. del Rosario*
Technological Support Center (CAT), Universidad Rey Juan Carlos, Móstoles, Spain

d *M. P. Morales, L. Gutiérrez*
Departamento de Biomateriales y Materiales Bioinspirados, Instituto de Ciencia de Materiales de Madrid, CSIC, Madrid, Spain

e *B. Galiana*
Physics Department, Universidad Carlos III, Av de la Universidad 40, 28911 Leganés, Madrid, Spain

hydrothermal synthesis through traditional protocols with reaction times lasting from 3 to 24 hours, making them unsuitable for radionuclide labeling with short-lived isotopes like ^{68}Ga. An alternative synthesis route for IONPs is microwave synthesis (MWS), which dramatically reduces reaction times, increases yields and enhances reproducibility (17–19), parameters of critical importance for the synthesis of IONP. The superior performance of MWS is due to dielectric heating: the rapid heating of the sample as the molecular dipoles try to align with the alternating electric field, with more polar solvents and reagents being more efficiently heated. Several reports have described MWS of Fe_2O_3 and Fe_3O_4 nanoparticles (20–24).

Radionuclide atoms can be attached to the nanoparticle either on the surface or by incorporation into the particle core. Most of the existing examples use surface attachment, either by passive adsorption or through the use of traditional chelators (25–31). The few examples that use a chelator-free approach restrict themselves to long-lived isotopes (30–32).The use of an isotope like ^{68}Ga with short half-live of 68 minutes is extremely challenging for nanoparticle core-labeling. We hypothesized that MWS would enable the fast incorporation of ^{68}Ga in the core of IONP in very short times, suitable for applications with short-lived radioisotopes such as ^{68}Ga, producing ^{68}Ga core-doped IONP (^{68}Ga-C-IONP). As important as a fast and reproducible synthesis of the core is the bioconjugation step particularly with an isotope as ^{68}Ga. With the use of MWS we have also rapidly attached 1,4-(butanediol) diglycidyl ether as linker and then conjugated a peptide in very short times and high yields. Finally, as an example of the possible applications of such nano-radiotracers we carried out the dual *in vivo* detection of angiogenesis, by functionalization of the ^{68}Ga-C-IONP with the well-known peptide RGD. The peptide, Arginine-glycine-aspartic acid peptide (RGD), binds to the $\alpha v\beta_3$ and $\alpha v\beta_5$ integrins that are overexpressed in nascent endothelial cells during angiogenesis in various tumors, and yet not in inactive endothelial cells, being a classical example for the detection of angiogenesis.

2. RESULTS AND DISCUSSION

2.1. Synthesis and characterization of ^{68}Ga-C-IONP

The complete synthesis of ^{68}Ga-C-IONP-RGD is depicted in scheme 1. The ^{68}Ga-C-IONP were synthesized by combining $FeCl_3$, dextran (6 KDa, selected because we were searching for a polymer large enough to ensure colloidal stability but not that large that it would increase too much the hydrodynamic size) and hydrazine hydrate in water with the eluate from a ^{68}Ge/^{68}Ga generator (as $^{68}GaCl_3$ in HCl 0.05M), and subjecting the mixture to very fast ramping (54 s) to 100 °C with MW irradiation at 240 W for 10 minutes. The particles were purified by gel filtration, and their physicochemical properties were studied. The elution profile of the column clearly shows two peaks corresponding to the nanoparticles and the free gallium (Fig. 1a). The gel filtration purification

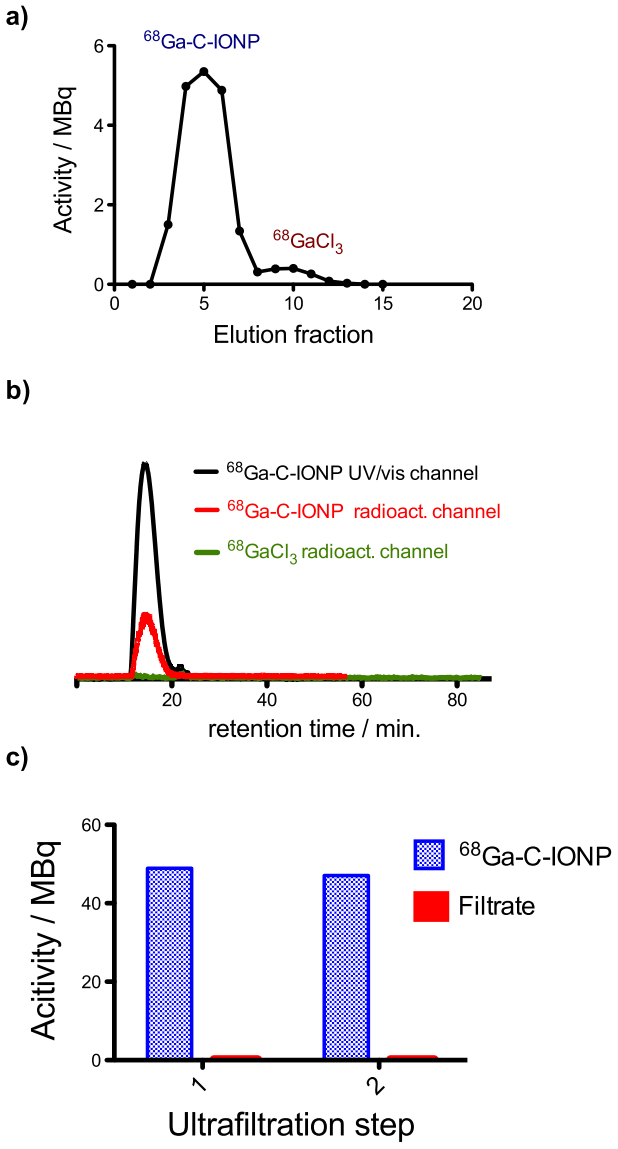

Figure 1. Radiochemical characterization of ^{68}Ga-C-IONP. (a) Gel filtration radio-chromatogram; (b) Chromatogram for ^{68}Ga-C-IONP in the UV channel at 380 nm (black line) and the radioactivity channel (red line), compared with the chromatogram for free ^{68}GaCl3 (green line) and (c) Activity measured, after incubation with mouse serum at 37 oC for 45 minutes, in two sequential ultracentrifugation steps in the particles and in the filtrate.

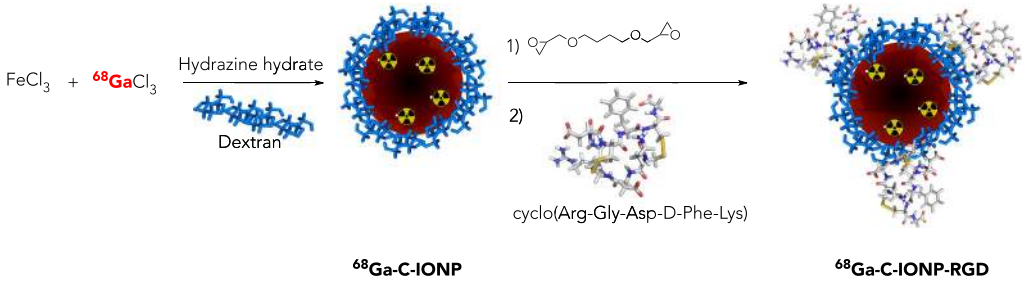

Scheme 1. Synthesis of ^{68}Ga core-doped iron oxide nanoparticles and functionalization with RGD peptide via 1,4-(butanediol) diglycidyl ether linker.

step also eliminates all unreacted $FeCl_3$, hydrazine and $^{68}GaCl_3$; however, due to its large size, excess dextran is co-eluted with the nanoparticles. The excess dextran was therefore removed in a second purification step, by ultrafiltration with a 100 KDa cut-off. The activity of incorporated ^{68}Ga was highly reproducible, after the purification steps, the mean radiolabeling yield was 93.4 ± 1.8 % (N=5, decay-corrected, 111 MBq initial dose). This exceptionally large value compares very favorably with the 33% of radiolabeling yield reported for ^{64}Cu incorporation.[25] Our procedure reproducibly provides 9 mL of ^{68}Ga-IONP with a high radiolabeling yield (Table S1) and 1.3 mg Fe/mL (Iron concentration was double checked by relaxometry and ICP measurements).

This high activity and iron oxide concentration provides the ideal combination for *in vivo* PET and MRI with the same nanoparticles. The protocol gave consistent results over a range of ^{68}Ga starting activities (37 MBq, 62.9 MBq, 111 MBq, 133.2 MBq, 1280 MBq) with no major effect on the main physicochemical properties (Table S1) including with the largest activity (1280 MBq) used for the *in vivo* experiment. The reproducibility of the method even with large amounts of incorporated ^{68}Ga extends the field of possible applications to include large animal models or humans. In addition to the two-step purification, we carried out standard gel-filtration HPLC quality-control checks for nano-radiochemicals. Chromatograms show that the radioactivity and nanoscale iron oxide have the same retention time, confirming the integration of the radioactive signal in the nanoparticles (Fig. 1b), moreover demonstrating that the radiation signal does not derive from the free radioisotope, which is not eluted quickly from these columns (green line in Fig. 1b). Finally we checked the stability of the labeling by incubating the ^{68}Ga-C-IONP with mouse serum at 37 °C during 45 minutes. Particles were afterwards purified by ultrafiltration and the activity checked in the filtrate. Figure 1c shows the results where it is clear that the activity remains in the particle even after the incubation period with no activity found in the filtrate.

After decay of the ^{68}Ga, the physicochemical properties of the nanoparticles were characterized; the synthesis yielded extremely small nanoparticles with a hydrodynamic size, determined by DLS, of 20.6 ± 2.4 nm (Fig. 2a). The DLS measurements also corroborate the high reproducibility of the method for 4 different repetitions of the reaction (Fig. 2b). TEM reported an extremely small core size of 2.2 ± 0.2 nm (average over 50 nanoparticles, Fig. 2c and Fig. S1). Surface composition was checked by FTIR and TGA showing a consistently high content of surface dextran, ensuring colloidal stability (Fig. 2d and 2e). FTIR showed the typical bands for dextran, particularly at 1000 cm^{-1}, and for iron oxide at 400 cm^{-1}. The large coating layer explains their good colloidal stability and also their relatively large hydrodynamic size (20.6 nm) compared to the core size (2.2 nm). The magnetic properties of iron oxide nanoparticles are dependent on the size of the crystalline core (26,27), and the very small size of ^{68}Ga-C-IONP particles therefore predicts a small magnetization saturation value.

The superparamagnetic behavior of the doped IONP was confirmed by analysis with a superconducting quantum interference device (SQUID), revealing a magnetic moment (Ms) of 19.2 emu/g Fe (Fig. 2g). To achieve optimal relaxivity as a T_1 MRI contrast agent, these nanoparticles must possess a high longitudinal relaxivity (r_1) and the lowest possible r_2/r_1 ratio (14). Measurement of relaxivity

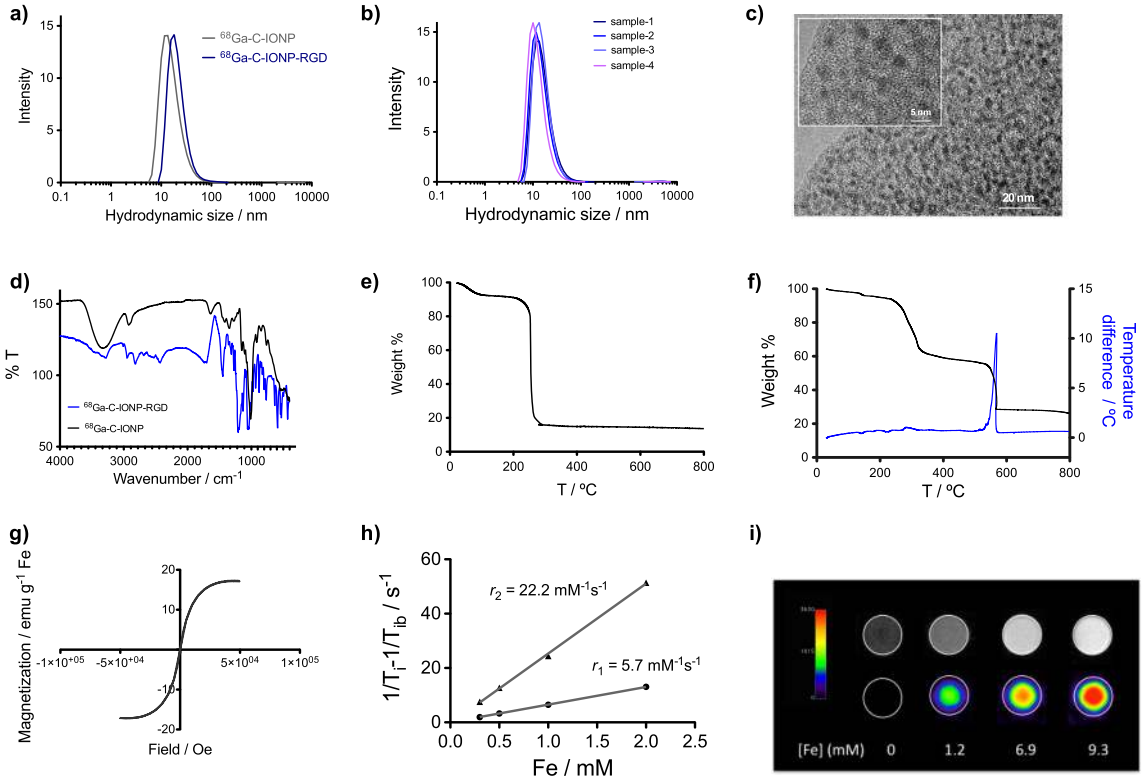

Figure 2. Physicochemical characterization of ^{68}Ga-C-IONP and ^{68}Ga-C-IONP-RGD. (a) Hydrodynamic size of ^{68}Ga-C- IONP and ^{68}Ga-C-IONP-RGD measured by DLS; (b) Hydrodynamic size of four different samples of ^{68}Ga-C- IONP; (c) TEM images at two magnifications of Hydrodynamic size of ^{68}Ga-C-IONP, (d) FTIR spectrum of ^{68}Ga-C-IONP; (e) Thermogravimetric curve of ^{68}Ga-C-IONP (f) Thermogravimetric curve of ^{68}Ga-C-IONP- RGD; (g) Field dependent magnetization of ^{68}Ga-C-IONP; (h) Plots of T_1 and T_2 relaxation rates against iron concentration for ^{68}Ga-C-IONP and i) Image phantoms obtained at different iron concentrations by MRI (top row) and PET (bottom row).

values for ^{68}Ga-C-IONP at 1.5 T and 37 °C revealed a very high value for r_1 of 5.7 $mM^{-1}s^{-1}$ and a modest r_2 value of 22.2 $mM^{-1}s^{-1}$ (Fig. 2h). This provides an r_2/r_1 ratio of 3.9, which should result in positive contrast. For example, clinically approved, Gd-based, Magnevist© and Omniscan© show r_1 values of 4.1 $mM^{-1}s^{-1}$, at 1.5 T, and 3.9 $mM^{-1}s^{-1}$ at 1.0 T, respectively. The high r_1 value of ^{68}Ga-C-IONP is attributable to the small size of the magnetic core, which leaves a large number of Fe^{3+} ions, each with five unpaired electrons, on the surface of the nanoparticle. To confirm the potential to generate positive contrast in MRI and PET signal with this new approach, phantoms with different iron concentration of ^{68}Ga-C-IONP were prepared. PET images and T_1-weighted MRI images (acquired 24 h later) both showed a correlation between signal intensity and the Fe content in the preparation, which in turn is directly associated with the amount of doped Gallium in the nanoparticle (Fig. 2i).

The demonstration that the ^{68}Ga was incorporated in the core has been carried out both by indirect radioactive methods and directly by EDS and XRF on Ga-C-IONP samples. First, we carried out our protocol but with a very different isotope, ^{18}F. As we had hypothesized, after the purification steps we obtained iron oxide nanoparticles with the same size and chemical properties, but with a 0.5% radiolabeling yield. The incorporation of this anionic isotope in the crystal structure of the IONP is more difficult and it would allow us to rule out any possible chances of adsorption of the radioisotopes on the surface of the nanoparticles or the polymeric matrix. To further confirm the presence of Ga in the core, Ga-C-IONP particles were prepared in a similar way and studied by polycrystalline diffraction, EDS and XRF. The continuous diffraction rings, in the diffraction study suggest a small grain size. The rings patterns were identified with X-ray diffraction patterns: PDF 01-074-2229 (ICSD name: Iron Gallium oxide, $FeGa_2O_4$) and PDF 00-019-0629 (Mineral name: Magnetite, Fe_3O_4). The chamber length was 730 mm. The local compositional analysis over particle was carried out by EDS spectra (Fig. S2). The compositional values have been calculated from the individual spectrum at each point; Ga is measured in the whole particle in a percentage of 0.22% in atomic composition. We also performed an X-ray fluorescence study, to get overall information regarding the presence of Ga. The percentage of Ga relative to Fe in this case is 0.294 ± 0.008%, in good agreement to the value obtained by EDS (Fig. S2). These data, together with the results from the reaction with ^{18}F and the stability of the labeling in serum clearly indicate that the Ga is incorporated in the IONP core and is not adsorbed into the polymeric layer.

2.2. Cytotoxicity experiments

In vitro toxicity tests of ^{68}Ga-C-IONP were carried out in two different human hepatoma cell lines (Huh7 and HepG2) and an endothelial cell line (EA.hy926) by image based high content analysis (Fig. S3). Cell counting showed that NP, unlike taxol treatment, did not affect cell viability. Fluorescent substrate for activated Caspases 3/7, which suffers translocation of cytoplasmic fluorescence signal to the nuclei in apoptotic cells revealed that NP did not elicit an apoptotic response, in contrast to taxol treated cells where the ratio of nuclei/cytoplasmic fluorescence was clearly increased in Huh7 and HepG2 cell lines (Fig. S3). Differences in Caspase cytoplasmic/nuclei translocation between control and NP (Fe-50 and Fe-20) in cell line Huh7 and control and NP (Fe-50) in cell line HepG2 were not statistically significant (independent 2-group Mann-Whitney U Test). Mitotracker dye that fluoresces when oxidized in actively respiring cells demonstrated that cells treated with NP, unlike taxol treated cells, were respiratory active at similar levels than control untreated cells (Fig. S3). Additionally, for the rest of conditions and measurements only small and medium effect size is shown for differences between NP and control (Cohen's d <0.5), while big effect size is shown for differences between taxol and control (Cohen's d >0.8). A noticeable reduction in the number of cells and a remarkable Caspase nucleus translocation was induced after taxol treatment but not by ^{68}Ga-C-IONP at concentrations as high as 100 μg/ml.

2.3. *In vivo* imaging with ^{68}Ga-C-IONP-RGD

Once the ^{68}Ga-C-IONP have been fully characterized, we functionalized them for the PET/MRI *in vivo* experiments as an example on the possible use of this new type of nano-radiotracer. RGD was coupled to the ^{68}Ga-C-IONP using the homobifunctional linker 1,4-(butanediol) diglycidyl ether (Scheme 1). Here again the use of MWS allowed the fast modification and conjugation of the nano-radiotracer. ^{68}Ga-C-IONP-RGD nanoparticles were purified by ultrafiltration obtaining particles with 390 MBq of activity (95% of radiolabeling yield). Size characterization of the vectorized nanoparticles by DLS (Fig. 2a) and TEM (Fig. S4) show no change in comparison to the initial ^{68}Ga-C-IONP. It is important to highlight that with the fast synthesis and conjugation we were able to produce nanoparticles with a good concentration for MRI experiments (19.7 mM Fe) and a very high radiolabeling yield (93.4%). Presence of RGD peptide was confirmed by FTIR, TGA and Bradford assay. The FTIR spectrum for ^{68}Ga-C-IONP-RGD (Fig. 2d) clearly shows the typical bands due to the incorporation of the peptide, like the broad band at 1693 cm^{-1} due to the peptide bond and the Arg side chain, the 1444 cm^{-1} due to the Lys side chain and at 1700 cm^{-1} and 1202 cm^{-1} due to the Asp side chain (33). Quantification of RGD reported 18.1 molecules of RGD per nanoparticle (quantified by Bradford analysis, assuming spherical shapes and 5.18 gcm^{-3} as the density for Fe_3O_4). TGA analysis also confirms the presence of a covalently attached molecule on the surface of the nanoparticles; it shows a 36% weight loss at 260 °C due to the dextran layer and a 30% weight loss at 550 °C with a strong heat development due to a covalently attached compound, the epoxide-RGD in this case. The ^{68}Ga-C-IONP-RGD agents were injected (15 MBq, 1.1 mg Fe/mL, 7.6 GBq/mmol, 100 μL), in tumor-bearing mice and imaging was taken 1 hour post-injection (PET/CT) and 24 hours (MRI) (Fig. 3, Fig. S5 and S6). PET imaging is particularly good with a clear signal in the tumor area (Fig. 3a) in all cases (N=5, tumor indicated with a white arrow in the CT image). MRI images also show a clear positive signal in the tumor area comparing the basal signal (Fig. 3d, left) with the same tumor after the injection (Fig. 3d, right) due to the good relaxometric values of ^{68}Ga-C-IONP-RGD (r_1 of 5.5 $mM^{-1}s^{-1}$ and r_2 of 20.7 $mM^{-1}s^{-1}$). To confirm that the accumulation was because of the presence of the RGD peptide several controls were performed. First, ^{68}Ga-C-IONP, without RGD, were injected in two tumor-bearing mice and PET/CT images taken 1 hour post-injection. A representative image is shown in Fig. 3b clearly demonstrating no accumulation in the tumor area (white arrow in the CT image) and some accumulation in the liver.

A second control consisted in a 'blocking' experiment (N=2) to demonstrate that the RGD functionality is the driven force for the accumulation. In this experiment RGD (1 mg) was injected previously (5 minutes) to the nanoparticles so it could block most of

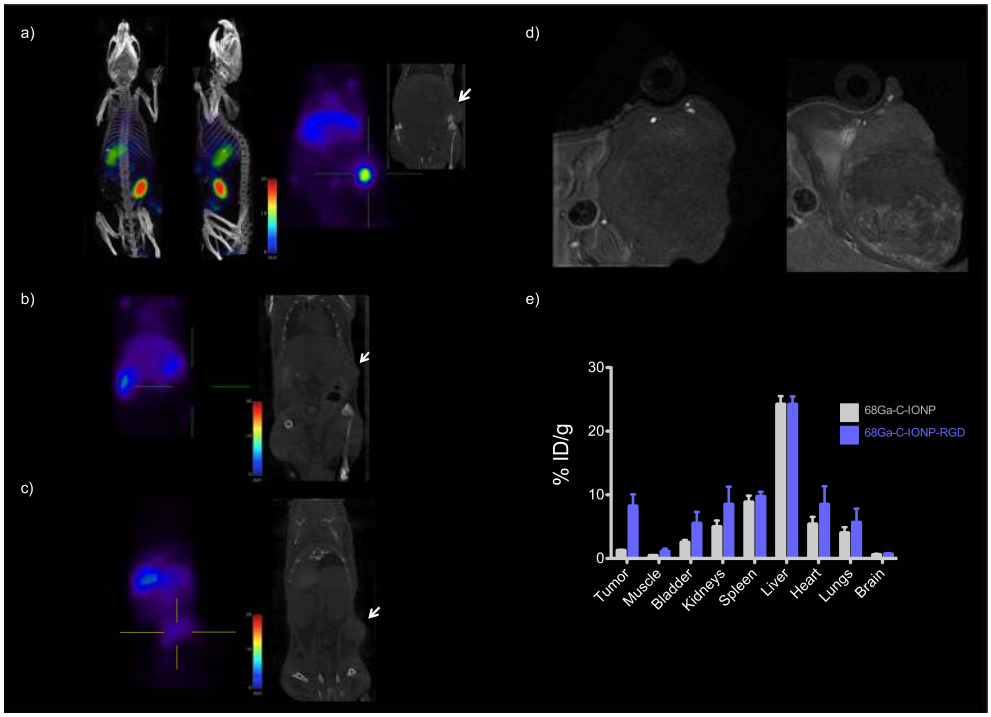

Figure 3. a) PET/CT imaging of tumor-bearing mice 1 hour after injection of ^{68}Ga-C-IONP-RGD, showing strong activity in the tumor; b) Control experiment, PET/CT imaging of tumor-bearing mouse 1 hour after injection of ^{68}Ga-C-IONP; c) Blocking experiment, PET/CT imaging of tumor-bearing mouse 1 hour after injection of RGD and then 68Ga-C-IONP-RGD d) Axial T_1 weighted spin echo MRI of the tumor area in a mouse previously to the injection of ^{68}Ga-C-IONP-RGD (left) and 24 hours post-injection (right) and e) Biodistribution of ^{68}Ga- C-IONP and ^{68}Ga-C-IONP-RGD after their administration in tumor-bearing mice, measured with a gammacounter (N=5).

the $\alpha_v\beta_3$ integrin binding sites and reduce or eliminate the accumulation of the ^{68}Ga-C-IONP-RGD. Images (Fig. 3c and Fig. S6) clearly displays that after the blocking the signal is reduced or completely eliminated in comparison to the initial experiment, confirming that the particles accumulate in the tumor because of the action of the RGD and not just a passive effect.

The final confirmation of these results came from the biodistribution study with gamma counter measurements (Fig. 3e). The biodistribution graph (N = 5) showing the percentage of injected dose per gram of organ for each particle clearly demonstrates the accumulation of the nanoparticles in the tumor and the typical accumulation in liver and spleen of these nanoparticles.

3. CONCLUSIONS

In this study, we describe a new iron oxide-based radiotracer nanoplatform. We demonstrate how microwave synthesis allows the reproducible and fast core-doping of the particles with an isotope such as ^{68}Ga, furthermore the nanoparticles perform quite well as positive contrast in MRI, joining the use of nanoradiotracers for T_1-MRI and ^{68}Ga-based PET without the use of traditional chelators. Both the methodology and the dual-modality platform will positively impact the field, opening the way to the synthesis of diverse libraries of compounds tailored to address different applications including treatment, pretargeted imaging and quantification of *in vivo* biological processes. As an example of the many possibilities we covalently modified the surface with an RGD moiety, via a homobifunctional linker. We show how this bioconjugation step can be performed very fast and with a high efficiency. The *in vivo* experiments clearly establish the accumulation in the tumor with both techniques and the selectively integrin binding to angiogenic endothelial cells.

4. EXPERIMENTAL

4.1. Synthesis of ^{68}Ga-C-IONP.

$FeCl_3$ x 6 H_2O (75 mg, 0.28 mmol), dextran (6 KDa, 140 mg, 0.02 mmol) and 1280 MBq of $^{68}GaCl_3$ in HCl (0.05 M, 3 mL) were dissolved in water (6 mL) in a microwave-adapted flask, followed by addition of 1 mL hydrazine hydrate. The solution was ramped to 100°C over 54 s and held at this temperature for 10 minutes (240 W) in a Monowave 300 (Anton Paar Germany GmbH73760 Ostfildern-Scharnhausen Germany, equipped with internal temperature probe and external IR probe). The reaction mixture was then cooled to 60°C and purified, first by passing through a PD-10 column to eliminate excess small reagents, including all unincorporated radiotracer, and second by ultrafiltration to remove unattached dextran. This purification process provided 9 mL of ^{68}Ga-C-IONP with a total activity of 781 MBq (measured 40 minutes after starting the reaction), a radiolabeling yield of 92%.

4.2. Synthesis of ^{68}Ga-C-IONP-RGD

To 2.5 ml of ^{68}Ga-C-IONP (770 MBq) were added 125 μl of a solution containing 0.6 M NaOH and 2 $mgml^{-1}$ of $NaBH_4$. Then, 0.68 mmol of 1,4-butanediol diglydicyl ether were put into the microwave adapted flask. The mixture was heated at 55 °C for 20 min in the microwave. The reaction was first purified by PD10-column using HEPES pH=8 buffer as eluent to remove

excess of reagents and secondly by ultrafiltration to remove possible undesirable cross-linked products. Non-filtrate was diluted to 2.5 with HEPES pH=8 buffer obtaining 521.8 MBq (measured after 35 min) with a radiolabeling yield of 97%. Then to 2.5 ml of ^{68}Ga-C-IONP-linker (515 MBq) suspended in HEPES pH=8 buffer were added 1 mg of c(RGDfK) dissolved in 200 μl of HEPES pH=8 buffer. The mixture was heated for 15 minutes at 55 °C in the microwave. Afterwards, the solution was purified by ultrafiltration to remove unattached c(RGDfK) and the non-filtrate redispersed in saline, obtaining an activity value of 390 MBq (measured after 25 min, 96%. 87% decay-corrected radiolabeling yield from initial reaction).

4.3. MRI relaxation properties of IONP samples.

Longitudinal and transverse relaxation times were measured for four concentrations of the nanoparticles in a Bruker Minispec (Bruker BioSpin GmbH 76189 Karlsruhe Germany) mq60 at 1.5 T and 37 °C with the standard Carr Purcell Meiboom Gill multi spin echo (T2) and Inversion Recovery spin echo (T1) sequences included in the system. R_1 and R_2 values were plotted against the Fe concentration in mM.

4.4. MRI and PET imaging

Mice were housed in specific facilities (pathogen-free for mice) at the Centro Nacional de Investigaciones Cardiovasculares. Experimental procedures were approved by the local Animal Care and Ethics Committee and regional authorities.

In vivo MRI in mice was performed with an Agilent/Varian scanner (Agilent, Santa Clara, CA, USA) equipped with a DD2 console and an active-shielded 205/120 gradient insert coil with 130 mT/m maximum gradient strength and a combination of volume coil/two channel phased-array (Rapid Biomedical GmbH, Rimpar, Germany). Mice (20 g) were anesthetized with 2% isoflurane and oxygen and positioned on a thermoregulated (38.7 °C) mouse bed. Ophthalmic gel was placed in their eyes to prevent retinal drying. Axial T1 weighted spin echo image were acquired with the following parameters: TR, 250 ms; TE, 8 ms, NA 8, Matrix 256 X 256, 30x30 mm FOV, 20 consecutive 0.5 mm slices and 125000 Hz spectral width.

In vivo PET/CT Imaging in mice was performed with a nanoPET/CT small-animal imaging system (Mediso Medical Imaging Systems, Budapest, Hungary). List-mode PET data acquisition commenced 1 hour post bolus injection of 15 MBq of ^{68}Ga-C-IONP through the tail vein and continued for 30 minutes. At the end of PET, microCT was performed for attenuation correction and anatomic reference. The dynamic PET images in a 105x105 matrix (frame rates: 3 x 10 minutes, 1 x 30 minutes, 1 x 60 minutes) were reconstructed using a Tera-Tomo 3D iterative algorithm. Acquisition and reconstruction were performed with proprietary Nucline software (Mediso, Budapest, Hungary). Qualitative Image analysis in mice was performed using Osirix software (Pixmeo, Switzerland).

In situ PET phantom imaging containing dilutions of ^{68}Ga-C-IONP was acquired during 15 minutes to observe the increasing signal in correlation with the PET activity and magnetic resonance imaging.

4.5. Peptide quantification by bradford analysis

Triplicates of ^{68}Ga-C-IONP-RGD and ^{68}Ga-C-IONP were prepared (2 μL), mixed with Bradford reagent (50 μL) and absorbance measured at 595 nm. BSA dilutions (0-15 μL, 1 mg/mL) were used as calibration.

4.6. Field dependent magnetization

Samples were prepared by adding 100 μL of the particle suspension to a piece of cotton wool. The solvent was then allowed to evaporate at room temperature overnight. The nanoparticle impregnated cotton was placed in a gelatine capsule, and field-dependent magnetization measurements were made with a MPMS-5S SQUID Magnetometer (Quatum Design) at 250 K up to 5 T.

4.7. Animal model

The subcutaneous model of melanoma was generated in 8-12-weeks old C57BL/6J males by injecting subcutaneously 50 0000 mouse melanoma cells (B16-F10 kindly provided by Dr. Manuel Serrano from CNIO). Animals were housed at 22 °C in a 12-hour light/dark cycle with water and food freely available. The animal procedures were carried in accordance with the legal regulations in Spain and the European Union (86/609/EC).

4.8. Quantitative toxicity assays

Human hepatocellular carcinoma cell lines Huh7, HepG2 and EA. hy926 were maintained in DMEM supplemented with 10% FBS. Cells were attached to 96 multiwell plates, then incubated with NP and Taxol for 24h in biduplicate wells, and fixed at RT for 15 min with 3% paraformaldehyde. Cells were stained with DAPI (4´, 6-diamidine-2-fenilindol), Mitotracker Orange and Cell Event 3/7 caspase Green for detection of nuclei, active respiratory cell mitochondria and apoptosis respectively. Staining reagents were all purchased from Invitrogen (Invitrogen, Carlsbad, CA, USA). Images, 35 per well, were acquired using an automated imaging system (Opera, Perkin Elmer, 940 Winter St. Waltham, Massachusetts 02451 USA) with a 20x objective. For reference, images of 2.5 mm multicolor beads, images of reference dyes and dark field images were collected using the Opera adjustment plate. Images were analysed using custom-designed algorithms within the Definiens Developer environment Definiens 7.0.2 (Definiens AG, Munich, Germany). First, a segmentation procedure based on automatic thresholding delimits the nuclei from the DAPI channel. The threshold is calculated using a combination of histogram-based methods that divide the complete set of pixels in DAPI signal into two subsets, so that heterogeneity is increased to a maximum. A watershed algorithm combined with a nuclei shape and size check strategy is then applied in order to assure the separation of adjacent nuclei. Once the nuclei are segmented, the algorithm grows the nuclear area outwards to delimit a cytoplasmic area. The growing algorithm is based on DAPI signal and it is constrained to a region around nuclei that fulfill several conditions based on a strategy of sequential intensity tolerances and surface tensions. Fluorescence mean intensity measurements both in nuclei and cytoplasm were obtained for the Mitotracker and caspase stainings. Caspase nuclear/cytoplasmic intensity ratio and Mytotracker cytoplasmic mean intensity were calculated for each cell. Number of nuclei were measured in different fields and averaged to obtain a per field quantification. The statistical significance comparing differences between the experimental and control was evaluated using independent 2-group Mann-Whitney U Test. All conditions showed significant statistical differences in Caspase ratios and Mitotracker intensities ($P<0.01$) between the experimental and control, except in Caspase ratios for control and NP (Fe-50 and Fe-20) in cell line Huh7 and control and NP (Fe-50) in cell line HepG2, where differences were not statistically significant. Moreover, small and medium effect size was shown

for differences between NP and control (Cohen's d <0.5) while big effect size was shown for differences between Taxol and control (Cohen's d >0.8).

Acknowledgments

This work was supported by a grant from Spanish ministry of economy (MAT2013-47303-P and SAF2012-1207), Fundació La Marató de TV3 (70/C/2012), by a grant from the Comunidad de Madrid (S2010/BMD-2326, Inmunothercan-CM and CAM/API1009). EA.hy926 cells were kindly provided by Dr. C-J. S. Edgell, University of North Carolina. We thank Irene Palacios Doiztua and Raquel Nieto from the Cellomic Unit and Marina Benito, Izaskun Bilbao and Coral Velasco for technical support. SC is recipient of a fellowship from the Marie Curie Actions – PEOPLE - COFUND Programme. The CNIC is supported by the Ministerio de Economía y Competitividad and the Pro-CNIC Foundation.

REFERENCES

1. Louie A. Multimodality imaging probes: design and challenges. Chem Rev 2010; 110: 3146–3195. doi:10.1021/cr9003538.
2. Pysz MA, Gambhir SS, Willmann JK. Molecular imaging: current status and emerging strategies. Clin Radiol 2010; 65: 500–516. doi:10.1016/j.crad.2010.03.011.
3. Judenhofer MS, Wehrl HF, Newport DF, Catana C, Siegel SB, Becker M, Thielscher A, Kneilling M, Lichy MP, Eichner M, Klingel K, Reischl G, Widmaier S, Röcken M, Nutt RE, Machulla HJ, Uludag K, Cherry SR, Claussen CD, Pichler BJ. Simultaneous PET-MRI: a new approach for functional and morphological imaging. Nat Med 2008; 14: 459–465. doi:10.1038/nm1700.
4. Cheng Z, Al Zaki A, Hui JZ, Muzykantov VR, Tsourkas A. Multifunctional nanoparticles: cost versus benefit of adding targeting and imaging capabilities. Science (80-) 2012; 338: 903–910. doi:10.1126/science.1226338.
5. Perez-Medina C, Abdel-Atti D, Zhang Y, Longo VA, Irwin CP, Binderup T, Ruiz-Cabello J, Fayad ZA, Lewis JS, Mulder WJ, Reiner T. A modular labeling strategy for in vivo PET and near-infrared fluorescence imaging of nanoparticle tumor targeting. J Nucl Med 2014; 55: 1706–1711. doi:10.2967/jnumed.114.141861.
6. Guo W, Sun X, Jacobson O, Yan X, Min K, Srivatsan A, Niu G, Kiesewetter DO, Chang J, Chen X. Intrinsically radioactive [64 Cu] CuInS/ZnS quantum dots for PET and optical imaging: improved radiochemical stability and controllable cerenkov luminescence. ACS Nano 2015; 9: 488–495. doi:10.1021/nn505660r.
7. Hu H, Huang P, Weiss OJ, Yan X, Yue X, Zhang MG, Tang Y, Nie L, Ma Y, Niu G, Wu K, Chen X. PET and NIR optical imaging using self-illuminating (64)Cu-doped chelator-free gold nanoclusters. Biomaterials 2014; 35: 9868–9876. doi:10.1016/j.biomaterials.2014.08.038.
8. Morgat C, Hindié E, Mishra AK, Allard M, Fernandez P. Gallium-68: chemistry and radiolabeled peptides exploring different oncogenic pathways. Cancer Biother Radiopharm 2013; 28: 85–97. doi:10.1089/cbr.2012.1244.
9. Vorster M, Maes A, Van deWiele C, Sathekge M. Gallium-68: a systematic review of its nononcological applications. Nucl Med Commun 2013; 34: 834–854. doi:10.1097/MNM.0b013e32836341e5.
10. Hu F, Jia Q, Li Y, Gao M. Facile synthesis of ultrasmall PEGylated iron oxide nanoparticles for dual-contrast T_1 - and T_2 -weighted magnetic resonance imaging. Nanotechnology 2011; 22. doi:10.1088/0957-4484/22/24/245604.
11. Yu T, Moon J, Park J, Park Y II, Na HB, Kim BH, Song IC, Moon WK, Hyeon T. Various-shaped uniform Mn_3O_4 nanocrystals synthesized at low temperature in air atmosphere. Chem Mater 2009; 21: 2272–2279. doi:10.1021/cm900431b.
12. Hannecart A, Stanicki D, Vander Elst L, Muller RN, Lecommandoux S, Thévenot J, Bonduelle C, Trotier A, Massot P, Miraux S, Sandre O, Laurent S. Nano-thermometers with thermo-sensitive polymer grafted USPIOs behaving as positive contrast agents in low-field MRI. Nanoscale 2015; 7: 3754–3767. doi:10.1039/C4NR07064J.
13. Taboada E, Rodríguez E, Roig A, Oró J, Roch A, Muller RN. Relaxometric and magnetic characterization of ultrasmall iron oxide nanoparticles with high magnetization. evaluation as potential T_1 magnetic resonance imaging contrast agents for molecular imaging. Langmuir 2007; 23: 4583–4588. doi:10.1021/la063415s.
14. Kim BH, Lee N, Kim H, An K, Park Y II, Choi Y, Shin K, Lee Y, Kwon SG, Na HB, Park J-G, Ahn T-Y, Kim Y-W, Moon WK, Choi SH, Hyeon T. Large-scale synthesis of uniform and extremely small-sized iron oxide nanoparticles for high-resolution T1 magnetic resonance imaging contrast agents. J Am Chem Soc 2011; 133: 12624–12631. doi:10.1021/ja203340u.
15. Xiao N, Gu W, Wang H, Deng Y, Shi X, Ye L. T1-T2 dual-modal MRI of brain gliomas using PEGylated Gd-doped iron oxide nanoparticles. J Colloid Interface Sci 2014; 417: 159–165. doi:10.1016/j.jcis.2013.11.020.
16. Szpak A, Fiejdasz S, Prendota W, Strączek T, Kapusta C, Szmyd J, Nowakowska M, Zapotoczny S. T1–T2 Dual-modal MRI contrast agents based on superparamagnetic iron oxide nanoparticles with surface attached gadolinium complexes. J Nanoparticle Res 2014; 16: 2678. doi:10.1007/s11051-014-2678-6.
17. Lidström P, Tierney J, Wathey B, Westman J. Microwave assisted organic synthesis –a review. Tetrahedron 2001; 57: 9225–9283. doi:10.1016/S0040-4020(01)00906-1.
18. Hayes BL. Microwave synthesis: chemistry at the speed of light. CEM Pub. 2002.
19. Pellico J, Lechuga-Vieco AV, Benito M, García-Segura JM, Fuster V, Ruiz-Cabello J, Herranz F. Microwave-driven synthesis of bisphosphonate nanoparticles allows in vivo visualisation of atherosclerotic plaque. RSC Adv 2015; 5: 1661–1665. doi:10.1039/C4RA13824D.
20. Acarbas O, Ozenbas M. Preparation of iron oxide nanoparticles by microwave synthesis and their characterization. J Nanosci Nanotechnol 2008; 8: 655–659.
21. Osborne EA, Atkins TM, Gilbert DA, Kauzlarich SM, Liu K, Louie AY. Rapid microwave-assisted synthesis of dextran-coated iron oxide nanoparticles for magnetic resonance imaging. Nanotechnology 2012; 23. doi:10.1088/0957-4484/23/21/215602.
22. Carenza E, Barceló V, Morancho A, Montaner J, Rosell A, Roig A. Rapid synthesis of water-dispersible superparamagnetic iron oxide nanoparticles by a microwave-assisted route for safe labeling of endothelial progenitor cells. Acta Biomater 2014. doi:10.1016/j.actbio.2014.04.010.
23. Bilecka I, Djerdj I, Niederberger M. One-minute synthesis of crystalline binary and ternary metal oxide nanoparticles. Chem Commun 2008: 886–888. doi:10.1039/B717334B.
24. Hu H, Yang H, Huang P, Cui D, Peng Y, Zhang J, Lu F, Lian J, Shi D. Unique role of ionic liquid in microwave-assisted synthesis of monodisperse magnetite nanoparticles. Chem Commun 2010; 46: 3866–3868. doi:10.1039/B927321B.
25. Choi J, Park JC, Nah H, Woo S, Oh J, Kim KM, Cheon GJ, Chang Y, Yoo J, Cheon J. A hybrid nanoparticle probe for dual-modality positron emission tomography and magnetic resonance imaging. Angew Chem Int Ed Engl 2008; 47: 6259–6262. doi:10.1002/anie.200801369.
26. Stelter L, Pinkernelle JG, Michel R, Schwartländer R, Raschzok N, Morgul MH, Koch M, Denecke T, Ruf J, Bäumler H, Jordan A, Hamm B, Sauer IM, Teichgräber U. Modification of aminosilanized superparamagnetic nanoparticles: feasibility of multimodal detection using 3T MRI, small animal PET, and fluorescence imaging. Mol Imaging Biol MIB Off Publ Acad Mol Imaging 2010; 12: 25–34. doi:10.1007/s11307-009-0237-9.
27. Glaus C, Rossin R, Welch MJ, Bao G. In vivo evaluation of 64Cu-labeled magnetic nanoparticles as a dual-modality PET/MR imaging agent. Bioconjug Chem 2010; 21: 715–722. doi:10.1021/bc900511j.
28. Nahrendorf M, Keliher E, Marinelli B, Leuschner F, Robbins CS, Gerszten RE, Pittet MJ, Swirski FK, Weissleder R. Detection of macrophages in aortic aneurysms by nanoparticle positron emission tomography –computed tomography. Arterioscler Thromb Vasc Biol 2011; 31: 750–757. doi:10.1161/ATVBAHA.110.221499.
29. Chen F, Ellison PA, Lewis CM, Hong H, Zhang Y, Shi S, Hernandez R, Meyerand ME, Barnhart TE, Cai W. Chelator-free synthesis of a dual-modality PET/MRI agent. Angew Chemie 2013; 52: 13319–13323. doi:10.1002/anie.201306306.
30. Zhao Y, Sultan D, Detering L, Cho S, Sun G, Pierce R, Wooley KL, Liu Y. Copper-64-alloyed gold nanoparticles for cancer imaging: improved

radiolabel stability and diagnostic accuracy. Angew Chemie Int Ed 2014; 53: 156–159. doi:10.1002/anie.201308494.
31. Chakravarty R, Valdovinos HF, Chen F, Lewis CM, Ellison PA, Luo H, Meyerand ME, Nickles RJ, Cai W. Intrinsically germanium-69-labeled iron oxide nanoparticles: synthesis and in-vivo dual-modality PET/MR imaging. Adv Mater 2014; 26: 5119–5123. doi:10.1002/adma.201401372.
32. Wong RM, Gilbert DA, Liu K, Louie AY. Rapid size-controlled synthesis of dextran-coated, ^{64} cu-doped iron oxide nanoparticles. ACS Nano 2012; 6: 3461–3467. doi:10.1021/nn300494k.
33. Barth A. The infrared absorption of amino acid side chains. Prog Biophys Mol Biol 2000; 74: 141–173.

SUPPORTING INFORMATION

Additional supporting information can be found in the online version of this article at the publisher's website.